Two-electron CO2 Reduction Reaction Mechanism on Nickel Cobalt Phosphate Surface Doped by Transition Metal: A DFT Study

Raka Primipara[1,2], Dzaki Ahmad Syaifullah[1], Muhammad Arkan Nuruzzahran[1], Dyah Puspasari Wijayanti[1,2], Hamad AlMohamadi[3], Nadhratun Naiim Mobarak[4], Fadjar Fathurrahman[1,5,6] , & Adhitya Gandaryus Saputro[1,5,6,*]

[1]Graduate Program of Engineering Physics, Faculty of Industrial Technology, Institut Teknologi Bandung, Jalan Ganesa No. 10, Bandung, West Java 40132, Indonesia
[2]PT. PLN (Persero), Kantor Pusat, Jalan Trunojoyo Blok M - I No. 135, DKI Jakarta 12160, Indonesia
[3]Department of Chemical Engineering, Faculty of Engineering, Islamic University of Madinah, Prince Naif Bin Abdulaziz Road, Al Jamiah, Madinah 42351, Saudi Arabia
[4]Department of Chemical Sciences, Faculty of Science and Technology, Universiti Kebangsaan Malaysia, Selangor 43600, Malaysia
[5]Quantum and Nano Technology Research Group, Institut Teknologi Bandung, Jalan Ganesa No. 10, Bandung, West Java 40132, Indonesia
[6]Research Centre for Nanoscience and Nanotechnology, Institut Teknologi Bandung, Jalan Ganesa No. 10, Bandung, West Java 40132, Indonesia

*Corresponding author: gandaryus@itb.ac.id

Abstract

In this study, we explore the activity and selectivity of the CO2 reduction reaction (CO2RR) to CO and HCOOH on pure and transition metal-doped NiCoPO(100) surfaces using density functional theory (DFT) calculations. The novelty of this work lies in demonstrating that substitutional doping with Mn, Fe, and Cu significantly alters the thermodynamic landscape of CO_2RR, particularly in enhancing selectivity toward HCOOH. While CO remains the dominant product on most surfaces, Mn-doped NiCoPO(100) uniquely reverses this trend by reducing the limiting potential for HCOOH formation to a value lower than that for CO production. Furthermore, Mn doping suppresses the competitive hydrogen evolution reaction (HER), steering the reaction pathway more selectively toward formic acid. These findings introduce Mn-doped NiCoPO as a promising and tunable catalyst platform for selective CO_2 to HCOOH conversion, providing valuable insights for designing efficient catalysts for sustainable carbon utilization.

Keywords: *CO₂ reduction reaction; DFT; HCOOH selectivity; Mn-doping effect; nickel cobalt phosphate; transition metal doping.*

Introduction

Climate change stands as one of the most pressing challenges of the 21st century, negatively affecting ecosystems, economies, and societies worldwide. The primary driver of global warming is the rise in greenhouse gas concentrations, particularly CO_2, resulting from fossil fuel combustion and industrial activities. This increase has led to significant alterations in weather patterns, rising sea levels, and a heightened frequency and severity of extreme weather events (Bolan et al., 2024; Moore et al., 2024; Shaikh et al., 2024). As a result, reducing CO_2 emissions has become a global imperative, essential for slowing climate change and ensuring environmental sustainability and future livelihoods.

Transforming CO_2 into value-added chemicals represents a promising complementary approach to addressing this issue. This technology allows CO_2, typically regarded as waste, to be converted into industrial chemicals, renewable fuels, and other synthesis materials, thereby fostering a more sustainable closed carbon cycle (Alli et al., 2023; Alli et al., 2024; Kumar & Eswari, 2023; Yusuf et al., 2023). One of the key methods for CO_2 conversion is the Carbon Dioxide Reduction Reaction (CO2RR), which facilitates the direct electrochemical transformation of CO_2 into multi-carbon products (Bi et al., 2018; Li et al., 2017; Peterson et al., 2010; Tripkovic et al., 2013). This method not only aids in mitigating CO_2

emissions but also aligns with the production of renewable chemicals and fuels, potentially utilizing electricity from renewable sources. However, significant challenges remain, including low product selectivity and a heavy reliance on the catalytic materials employed (Li et al., 2017; Yang et al., 2024).

Despite its potential as a solution to the global CO_2 dilemma, technology faces significant challenges that limit its efficiency and practical implementation. These include poor product selectivity and a reliance on specific catalytic materials. Although noble metal catalysts such as silver (Ag) and gold (Au) exhibit excellent performance in CO_2RR, their high cost and limited availability remain major barriers to widespread adoption (Huang et al., 2019; Li et al., 2021; Ma et al., 2022; Ma et al., 2023). To overcome these limitations, increasing research efforts have been devoted to developing non-precious metal catalysts that offer both low cost and high catalytic activity. It is now widely recognized that such catalysts can achieve excellent selectivity and efficiency through strategies such as nanostructure engineering, heteroatom doping, and alloying with other transition metals (Li et al., 2017; Maulana et al., 2019; Maulana et al., 2021; Nuruddin et al., 2023; Nuruddin et al., 2024; Saputro et al., 2021a; Saputro et al., 2021b). These approaches modify the electronic and geometric properties of the active sites, thereby enhancing CO_2 adsorption and facilitating its electrochemical conversion.

Nickel-based catalysts have emerged as highly promising materials for the electrochemical reduction of CO_2, particularly toward the formation of C_1 products (Liu et al., 2023). Nickel in the form of nanoparticles (He et al., 2022; Niu et al., 2021; Tan et al., 2019; Xu et al., 2020), and compounds such as nitrides (Zhao et al., 2023; Hou et al., 2018) and chalcogenides (Han et al., 2022; Saxena et al., 2022) has been demonstrated to efficiently generate C_1 products, predominantly CO, with Faradaic efficiencies exceeding 80%. Moreover, Ni single-atom catalysts anchored on carbon frameworks demonstrate enhanced activity and selectivity toward CO production, even under industrially relevant current densities (Chen et al., 2023; Hua et al., 2022; Jeong et al., 2019; Zhao et al., 2021; Zheng et al., 2019). These advancements highlight the strong potential of Ni-based materials for driving the CO_2RR process, while underscoring the need to explore novel Ni-containing compounds to further enhance catalytic activity and product selectivity.

In recent years, bimetallic nickel phosphate materials, particularly NiCo phosphate, have demonstrated remarkable performance in various electrochemical applications, such as the hydrogen evolution reaction, oxygen evolution reaction, supercapacitors, and electrochemical sensors (Darminto et al., 2025; El-Gohary et al., 2023; Ikhwan et al., 2025; Li et al., 2021; Nuruzzahran et al., 2025; Qian & Miao, 2019; Septiani et al., 2020a; Septiani et al., 2020b; Syaifullah et al., 2026; Wang et al., 2021; Wijayanti et al., 2025; Zhang et al., 2019; Zhang et al., 2022; Zhao & Yuan, 2020; Zhou et al., 2019). Despite these advances, their potential as electrocatalysts for the CO_2 reduction reaction (CO_2RR) remains largely unexplored. In this work, we explore the catalytic performance of NiCo phosphate in a 1:1 ratio [$Ni_3Co_3(PO_4)_4$, or simply NiCoPO] along with transition metal-doped variants (NiCoPO-M, where M = Mn, Fe, and Cu) using density functional theory (DFT) calculations. Our focus is on their ability to catalyze the two-electron CO_2RR to produce CO and formic acid (HCOOH). We anticipate that incorporating M dopants will modify product selectivity and enhance the catalytic activity of the surfaces, leading to improved efficiency in the CO_2RR process.

Computational Details

The Density Functional Theory (DFT) calculations in this study were conducted using the Quantum Espresso package (Giannozzi et al., 2009). The interaction between valence electrons and ionic reality is represented by the ultra-soft pseudopotential (Maulana et al., 2021). The exchange and correlation effects were addressed within the generalized gradient approximation (GGA) using the Perdew-Burke-Ernzerhof (PBE) functional (Perdew et al., 1996). For consistency with our previous studies on electrocatalysts, van der Waals interactions were treated using the semi-empirical DFT-D2 method developed by Grimme (Grimme, 2006).

Experimentally, the active facet of NiCoPO responsible for electrocatalytic performance has not yet been identified. In our previous work, the most stable NiMPO(100) surface was used as a model to study the OER activity of bimetallic NiMPO, and the calculated trends showed good agreement with experiments (Nuruzzahran et al., 2025). Following this rationale, in the present study we also adopt the (100) facet for modeling NiCoPO and NiCoPO–M surfaces to investigate the CO_2RR mechanism. It should be noted that while other facets may also exhibit distinct catalytic behaviors, the present investigation is limited to the (100) facet.

The bottom two $Ni_3Co_3(PO_4)_4$ layers were fixed to simulate bulk conditions, while the top layer was allowed to fully relax. The dimensions and structure of the unit cell used for this modeling are shown in Figure 1. The Brillouin zone was sampled at the gamma point due to the large unit cell size, with a kinetic energy cutoff of 50 Ry and a density cutoff of 500 Ry to ensure accurate calculations of wavefunction and charge density (Nuruzzahran et al., 2025). A 15 Å vacuum

was added to prevent interactions between periodic images, and dipole corrections were applied to address potential asymmetry in charge distribution. The system was relaxed until the residual forces on each atom were below 0.025 eV/Å. For isolated molecule calculations, a 30 Å x 30 Å x 30 Å cubic cell at the gamma point cell was used (Li et al., 2024).
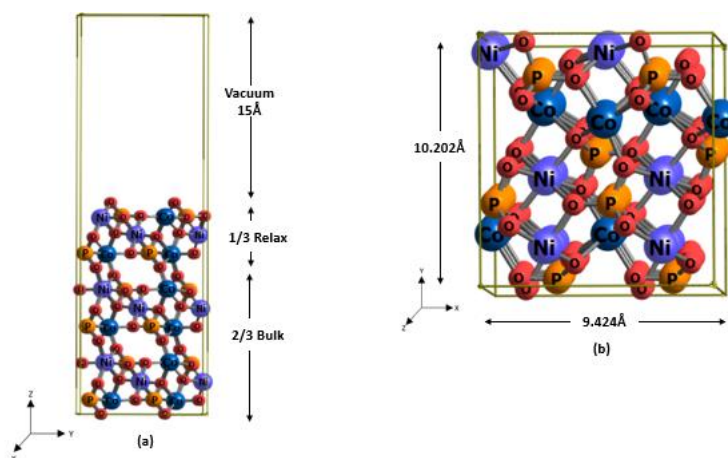

Figure 1   (a) Side view and (b) top view of NiCoPO (100).

The adsorption energy of an adsorbate on the active site of the NiCoPO(100) and NiCoPO(100)-M surfaces is calculated using the following relation:

$$E_{ads} = E(^*X) - (E(^*) + E(X)) \tag{1}$$

$E(^*X)$, $E(^*)$, and $E(X)$ represent the DFT total energies of an X species adsorbed on the surface, a clean surface, and an isolated X species, respectively.

We approximated the change in free energy of the basic electrochemical processes involved in the CO₂RR process using the computational hydrogen electrode (CHE) model (Norskov et al., 2004). Using the standard hydrogen electrode (SHE), the chemical potential of $\frac{1}{2}$ H₂ gas is related to the free energy of the [H⁺+e⁻] reaction under standard conditions. The following relation is used to determine the change in free energy for *A + H⁺ + e⁻ (U) → *AH elementary step at a given electrode potential U (ΔG(U)).

$$\Delta G(U) = E(^*AH) - (E(^*A) - \frac{1}{2}E(H_2) + \Delta ZPE - T\Delta S - \text{pH } k_b \text{ T ln } 10 + eU) \tag{2}$$
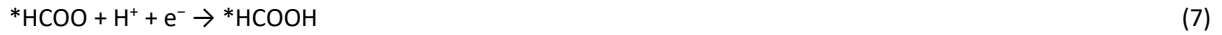
The changes in zero-point energies and entropies are represented by ΔZPE and Δ*S*, respectively. The NIST database provided the ZPE and *S* values for the CO₂RR intermediates. The ZPE was calculated as $\text{ZPE} = \frac{1}{2}\sum_i h\nu_i$, where ν_i corresponds to the vibrational frequency of mode i. We applied the following correction for the PBE functional to account for the error in reaction energies from periodic DFT calculations (Blaylock et al., 2009; Calle-Vallejo et al., 2011; Peterson et al., 2010). For CO₂ and CO molecules, the enthalpic corrections are +0.17 and −0.30 eV, respectively (Maulana et al., 2021). In order to approximate the solvent interaction with the OH group of OH-containing intermediates, we additionally include a correction of −0.30 eV (Kim et al., 2017; Tripkovic et al., 2013). We also performed microkinetic simulations to calculate the turnover frequencies (TOFs) of the CO₂RR pathways, using the Gibbs free energies of the elementary reactions as input parameters. The detailed derivation of the microkinetic model is provided in our previous publications (Maulana et al., 2021; Saputro et al., 2021a; Saputro et al., 2021b).

One common method for comparing the electrochemical process performance of some active site systems is by using the value of limiting potential (U_L). At a potential greater than the U_L, the reaction rate drastically drops. U_L is defined as $U_L = -\Delta G_{max}/e$ in the CHE approximation, where ΔG_max is the maximum free energy of a given reaction pathway at its equilibrium potential. When a system's U_L is higher, its electrochemical activity for a given reaction pathway is typically better than that of other systems. Unfortunately, this parameter is not particularly useful for assessing the performance of a CO₂RR process due to the selectivity issue from the parasitic HER process. Therefore, a more effective metric is the limiting potential difference between the CO₂RR and HER processes, represented as ΔU_L = U_L (CO₂RR)−U_L (HER) (Bi et al., 2018; Kim et al., 2017; Li et al., 2017). A more positive ΔU_L signifies enhanced selectivity toward CO₂RR.

In this work, we focus on the two-electron CO₂ reduction reaction (CO₂RR) pathways that lead to the production of carbon monoxide (CO) and formic acid (HCOOH). Both CO and HCOOH are produced through distinct sets of elementary reaction steps (Maulana et al., 2021). The reduction of CO₂ to CO typically follows these steps:

$$CO_{2(g)} + H^+ + e^- + * \rightarrow *COOH \tag{3}$$

$$*COOH + H^+ + e^- \rightarrow *CO + H_2O_{(l)} \tag{4}$$

$$*CO \rightarrow CO_{(g)} + * \tag{5}$$

where * and *X corresponds to an empty active site and an adsorbed X species on the active site. For the formation of HCOOH, the elementary reactions are as follows:

$$CO_{2(g)} + H^+ + e^- + * \rightarrow *HCOO \tag{6}$$

$$*HCOO + H^+ + e^- \rightarrow *HCOOH \tag{7}$$

$$*HCOOH \rightarrow HCOOH_{(aq)} + * \tag{8}$$

The key difference between these two pathways lies in the intermediates involved: CO production proceeds via a carboxyl intermediate (COOH), while HCOOH formation involves a format intermediate (HCOO).

Additionally, the parasitic hydrogen evolution reaction (HER), which competes for protons and electrons to form H_2, is assumed to follow this mechanism:

$$H^+ + e^- + * \rightarrow *H \tag{9}$$

$$H^+ + e^- + *H \rightarrow H_{2(g)} + * \tag{10}$$

Step (9), known as the Volmer step, involves the adsorption of hydrogen atoms (*H) onto the catalyst surface via protons present in the electrolyte. Step (10), known as the Heyrovsky step, involves the bonding of another proton with the adsorbed *H to produce H_2. Together, these two steps constitute the Volmer-Heyrovsky mechanism (Ferriday et al., 2021).

Results

Formation energy of surface doping

In this study, transition metals (Mn, Cu, and Fe) were doped into the NiCoPO(100) surface by substituting one of the top-layer Ni or Co atoms with a dopant atom (M). As an illustration, in the case of Mn-doped NiCoPO(100), an Mn atom can replace a surface Ni atom (denoted as NiCoPO(100)-Mn@Ni, see Figure 2a) or a surface Co atom (denoted as NiCoPO(100)-Mn@Co, see Figure S5a of Supporting Information). The formation energy for this substitution is calculated using the equation:

$$E_{form} = E(NiCoPO\text{-}M) - (E(NiCoPO) + \mu_M - m\mu_{Ni} - n\mu_{Co}) \tag{11}$$

$E(NiCoPO\text{-}M)$, $E(NiCoPO)$, and μ_i represent the total energies of the NiCoPO–M surface, the pristine NiCoPO surface, and the chemical potential of metal i, respectively. The chemical potential of Mn is taken from body-centered cubic (BCC) Mn, Fe from BCC Fe, Co from face-centered cubic (FCC) Co, Ni from FCC Ni, and Cu from FCC Cu. value of m and n depends on the substitution site of the M atom. For doping at the Co site, m = 0 and n=1, while for doping at the Ni site, m=1 and n=0. The formation energies for all doping systems on the NiCoPO(100) surface, considering both Ni and Co substitution sites, are presented in Table 1.

Table 1 Doping formation energy on NiCoPO(100) surface.

System	Formation Energy (eV)
NiCoPO(100) -Mn@Ni	-2.18
NiCoPO(100) -Mn@Co	-1.87
NiCoPO(100) -Fe@Ni	-1.11
NiCoPO(100) -Fe@Co	0.57
NiCoPO(100) -Cu@Ni	-0.39
NiCoPO(100) -Cu@Co	-0.08

The formation energy differs between substitutions at the Ni and Co sites, with nearly all values being negative, indicating that the doping process is energetically favorable. The results consistently show that the formation energy for substitutions at the Ni site is more negative than at the Co site, suggesting that doping at the Ni site is more stable. Consequently, this study focuses on the substitution of Mn, Fe, and Cu atoms at the Ni site only. Figure 2 illustrates the most stable doping configurations for each metal.
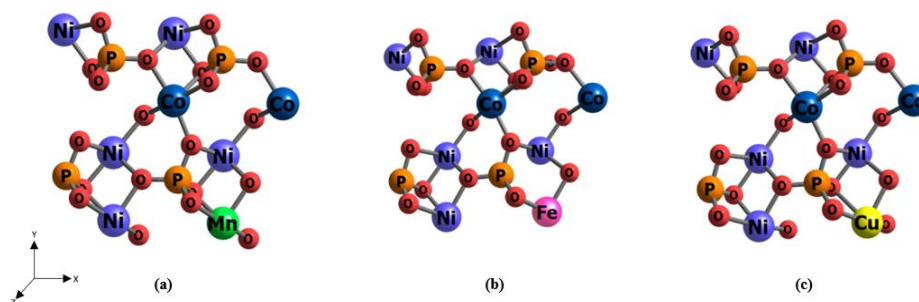
Figure 2   Top view of (a) NiCoPO(100)-Mn@Ni, (b) NiCoPO(100)-Fe@Ni (c) NiCoPO(100)-Cu@Ni.

CO₂ Adsorption

The initial step in the CO₂RR process involves the adsorption of CO₂ molecules at the catalyst's active sites. Table 2 and Figure 3 provide the adsorption energies, geometrical parameters, and the amount of charge transferred to the adsorbed CO₂ molecule. The data show that CO₂ binds to the metal sites with a bond distance greater than 2 Å and exhibits minimal charge transfer, indicating weak interaction. Moreover, the geometrical parameters reveal that the adsorbed CO₂ maintains its linear gas-phase structure, strongly suggesting that CO₂ is adsorbed in a physisorption state on most of the active sites of both NiCoPO(100) and NiCoPO(100)-M surfaces. The only exception is the Cu site on the NiCoPO(100)-Cu@Ni surface, where CO₂ fails to bind effectively, indicating that this site likely has low CO₂RR activity. Therefore, the CO₂RR at the Cu site will not be further considered in this study.

The physisorption state of CO₂ molecule can also be seen in the profile of the local density of states (LDOS) for the CO₂ adsorption on the catalyst. Figure 4 shows the LDOS for CO₂ adsorption on the Mn site of NiCoPO(100)-Mn@Ni surface. It is very clear that the π-orbitals of the adsorbed CO₂ (HOMO) only getting slightly broadened due to polarization from the surface without experiencing any orbital splitting after in contact with the *d*-orbitals of the Mn atom. The absence of orbital splitting clearly indicates that the adsorbed CO₂ is in the physisorption state.

Table 2 and Figure 3 show that the CO₂ molecule binds exclusively to the surface metal sites across all surfaces, with no significant differences in adsorption energy due to the physisorption state. This suggests that the CO₂RR process can be initiated with similar probabilities on all NiCoPO(100) and NiCoPO(100)-M active sites. Consequently, each catalyst system exhibits a range of limiting potential values arising from the contributions of multiple active sites, rather than a specific value attributed to a single site.

Table 2   Parameters of CO₂ adsorption on the NiCoPO(100) and NiCoPO(100)-M surfaces.

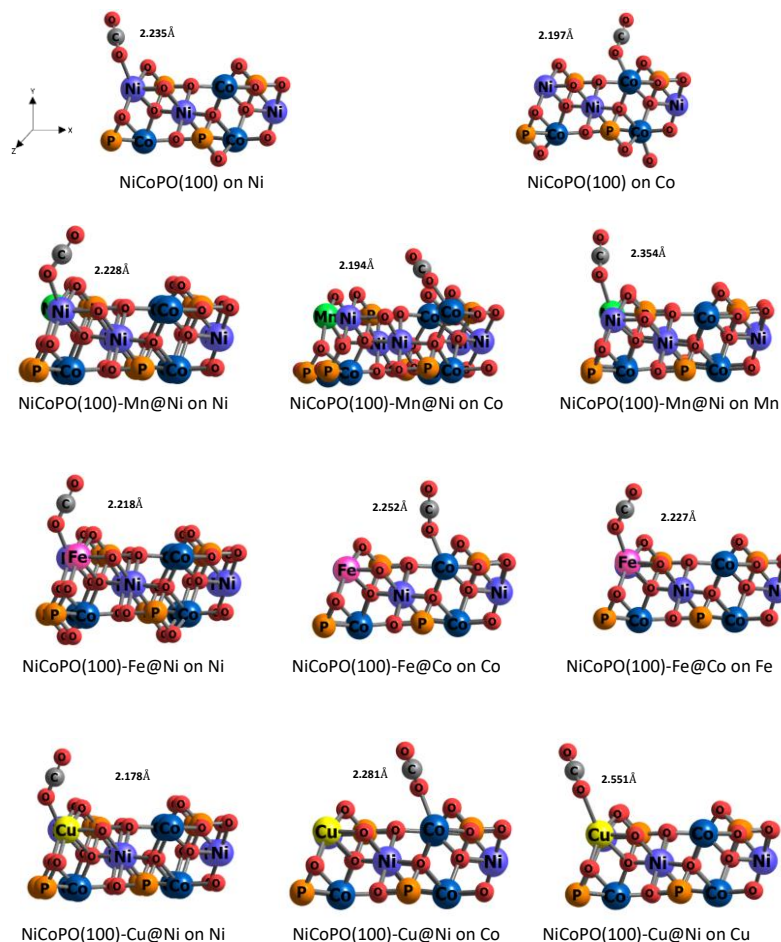| System	Site	$M - CO_2$ (Å)	O-C-O (º)	ΔQ(e)	$E_{ads}^{CO_2}$(eV)
NiCoPO(100)	Ni	2.235	178.81	-0.02	-0.06
	Co	2.197	177.03	-0.00	-0.19
NiCoPO(100)-Mn@Ni	Ni	2.228	178.39	-0.01	-0.14
	Co	2.194	176.24	0.00	-0.25
	Mn	2.354	178.99	-0.01	-0.23
NiCoPO(100)-Fe@Ni	Ni	2.218	178.48	-0.01	-0.09
	Co	2.252	178.86	-0.01	-0.08
	Fe	2.227	176.51	-0.00	-0.22
NiCoPO(100)-Cu@Ni	Ni	2.178	177.02	-0.01	-0.16
	Co	2.281	179.15	-0.01	-0.07
	Cu	2.551	179.21	-0.00	0.04

Figure 3   The geometry of CO_2 adsorption on the catalyst surface.
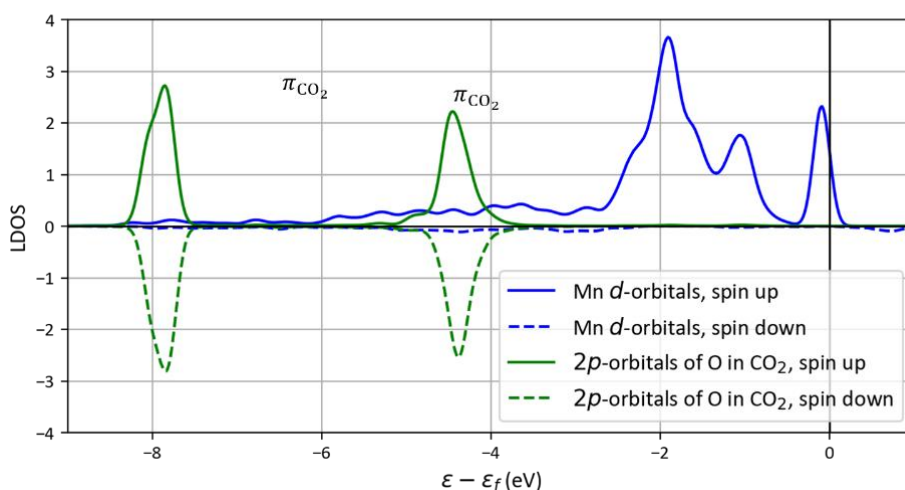

Figure 4   LDOS of CO_2 adsorption on Mn site of NiCoPO(100)-Mn@Ni surface

CO₂RR to CO

After confirming that CO_2 gas can bind to the transition metal sites of the NiCoPO(100) and NiCoPO(100)-M surfaces, we proceed to analyze the CO₂RR process at these sites. We begin with the CO_2 reduction to CO, which follows the sequence of elementary electrochemical reactions (3)-(5). Figure 4 illustrates the energy profile of the CO formation

reaction at the active sites of NiCoPO(100) and NiCoPO(100)-M surfaces. This diagram offers detailed insights into the energy changes during each reaction step, enabling a comparative analysis of the various catalyst systems with regard to their CO formation efficiency. The detailed free energy values and adsorption geometries of intermediates are provided in Table S1 – S6 and Figure S1 – S4 of Supporting Information.
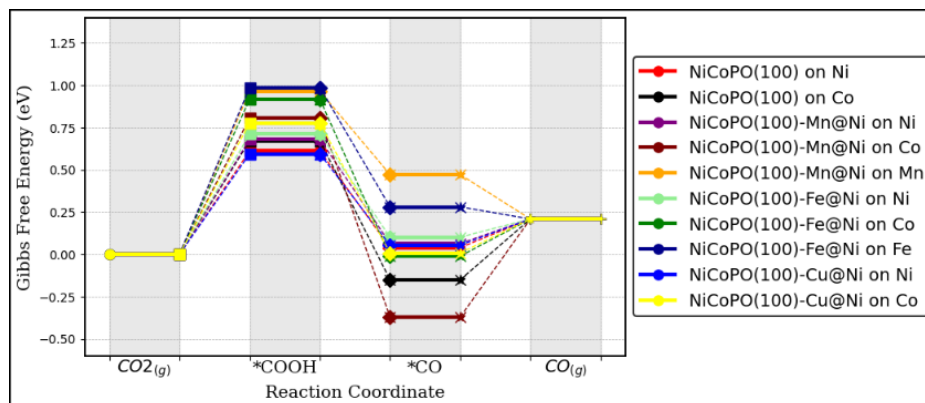

Figure 5   Free energy profiles for CO_2RR to CO.

Table 3   Thermodynamics determining steps (TDS) and limiting potential U_L for CO_2RR to CO.

System	Site	TDS	U_L (V)
NiCoPO(100)	Ni	(3)	-0.61
	Co	(3)	-0.67
NiCoPO(100)-Mn@Ni	Ni	(3)	-0.68
	Co	(3)	-0.80
	Mn	(3)	-0.96
NiCoPO(100)-Fe@Ni	Ni	(3)	-0.71
	Co	(3)	-0.91
	Fe	(3)	-0.98
NiCoPO(100)-Cu@Ni	Ni	(3)	-0.59
	Co	(3)	-0.77

From Figure 5, it is evident that transition metal doping can alter the Gibbs energy profile for CO formation on the NiCoPO(100) surface. The limiting potential (U_L), presented in Table 3, represents the minimum electrochemical potential below which the CO_2RR begins to proceed. This parameter is crucial for assessing the activity of various electrochemical catalysts. The data indicates that, generally, the lowest limiting potential for CO formation on both pure and doped NiCoPO(100) surfaces occurs at the Ni site.

However, the introduction of dopants has not significantly reduced the limiting potential for CO formation. A shift toward a more positive potential, relative to the pure NiCoPO(100) surface, is only observed at the Ni site of the NiCoPO(100)-Cu@Ni surface. This suggests that transition metal doping (Mn, Fe, and Cu) does not substantially influence the CO_2RR activity for CO formation in the NiCoPO(100) system.

Interestingly, the thermodynamic determining step (TDS) for this conversion process consistently originates from the COOH formation step, which exhibits an endothermic profile (reaction 3), as detailed in Table 3. This finding indicates that the COOH formation step can serve as a key descriptor for explaining the activity trend of CO formation in the system under study.

Figure 6 illustrates the relationship between E_{ads}^{COOH} and U_L for CO production. While the Co site of NiCoPO(100) exhibits some deviation, the overall trend clearly shows that stronger COOH adsorption energies are associated with lower U_L values for CO production. However, for most NiCoPO(100)-M surfaces, the COOH adsorption energies are weaker than those of the pristine NiCoPO(100) surface, indicating that introducing transition metal dopants (Mn, Fe, and Cu) does not effectively lower the U_L for CO production pathway.

The observed activity trend can be rationalized by analyzing the electronic structure of the isolated COOH intermediate and the NiCoPO(100)-M surfaces. Figure 7a presents the localized density of states (LDOS) of the COOH molecule. Particular attention is given to the frontier molecular orbitals with predominant p-orbital character on the carbon atom,

since COOH adsorption primarily involves bond formation between the carbon atom in COOH and the transition metal atom on the surface (see Figures S1–S4 in the Supporting Information). Based on this criterion, the α/β-HOMO and α-HOMO-2 orbitals are primarily responsible for COOH adsorption. These orbitals, particularly α-HOMO-2 and β-HOMO, are located relatively far from the Fermi level. Therefore, the surface states that interact with these orbitals must also lie within a comparable energy range to enable effective orbital hybridization. Figure 8 presents the d-orbital profiles of the NiCoPO(100)-M surfaces. It is evident that the *d*-orbitals of the Ni and Co sites on both pristine and doped NiCoPO(100) surfaces occupy a similar energy range, whereas those of the transition metal–doped sites, especially in the spin-down channel, are generally clustered at higher energy levels. Consequently, the *d*-orbitals of the Ni and Co sites interact more effectively with the carbon-localized frontier orbitals of COOH than those of the transition metal–doped sites. As a result, the COOH adsorption energies at the doped sites are weaker than at the Ni and Co sites. This finding explains why transition metal doping does not significantly enhance COOH adsorption. Furthermore, the similarity in *d*-orbital profiles between the Ni and Co sites accounts for the clustering of COOH adsorption energies within a narrow range across all surfaces.
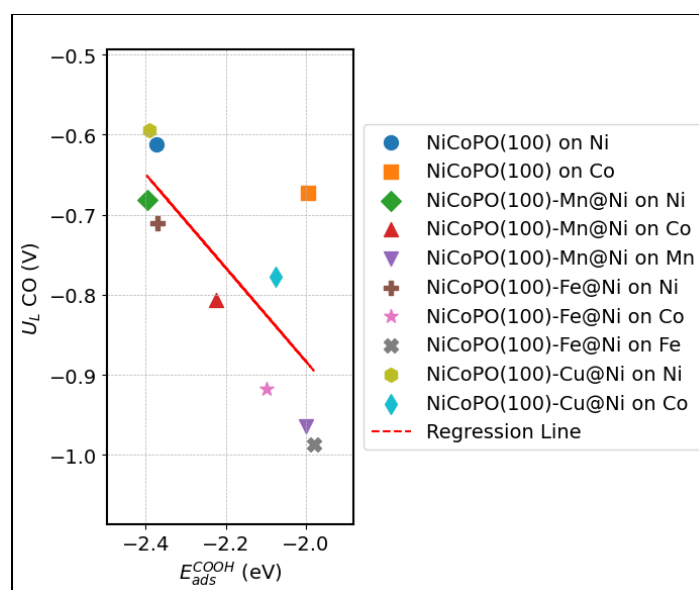

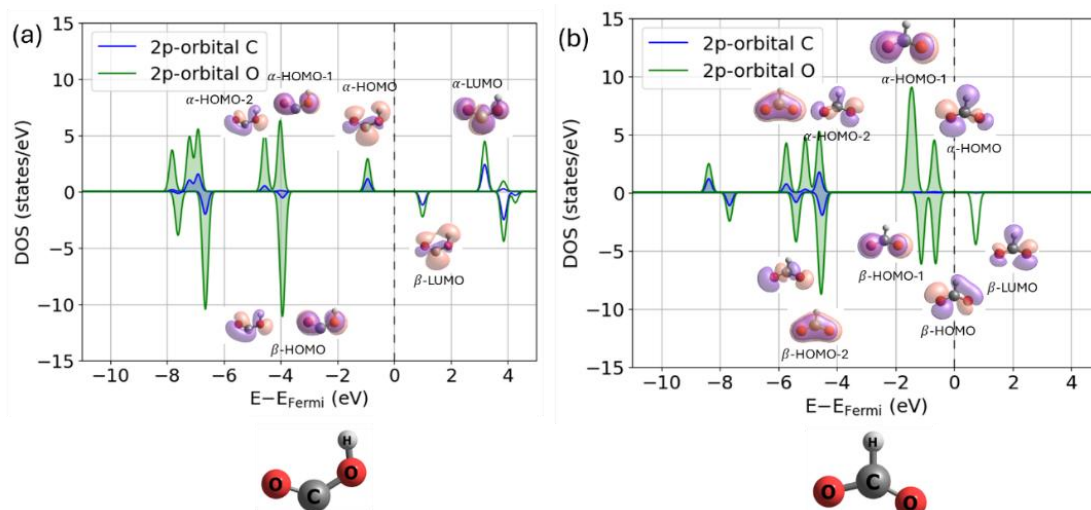**Figure 6** Relation between E_{ads}^{COOH} vs U_L for CO_2RR to produce CO.

Figure 7 Molecular orbitals of isolated (a) COOH and (b) HCOO intermediates. Shaded area indicating occupied states below the Fermi level.
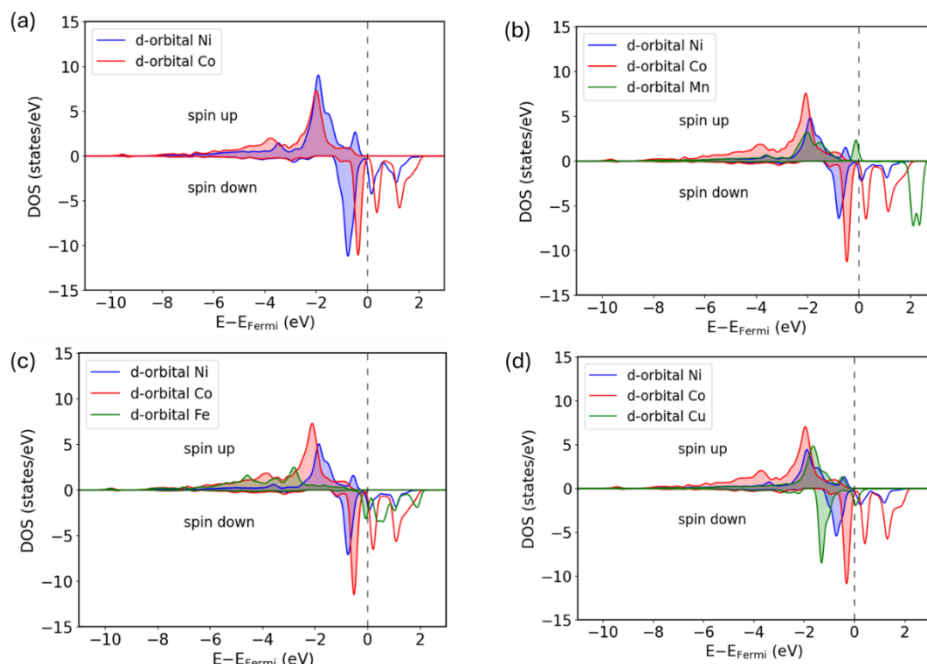
Figure 8 LDOS of (a) NiCoPO(100), (b) NiCoPO(100)-Mn, (c) NiCoPO(100)-Fe, and (d) NiCoPO(100)-Cu. The shaded area indicating occupied states below the Fermi level.

The TOF profiles for the CO_2RR to CO pathway obtained from microkinetic simulations are presented in Figure 9a. The TOF increases sharply at a certain potential, indicating the onset of CO_2 reduction, which is closely related to the calculated U_L values in Table 3. To compare the activity across different sites, we extracted the TOF at -0.6 V and correlated it with the descriptors of limiting potential for CO_2RR to CO, as shown in Figure 9b. The results are consistent with the general trend predicted by the U_L values in Figure 6, namely that stronger COOH adsorption energies correspond to higher CO_2RR activity.
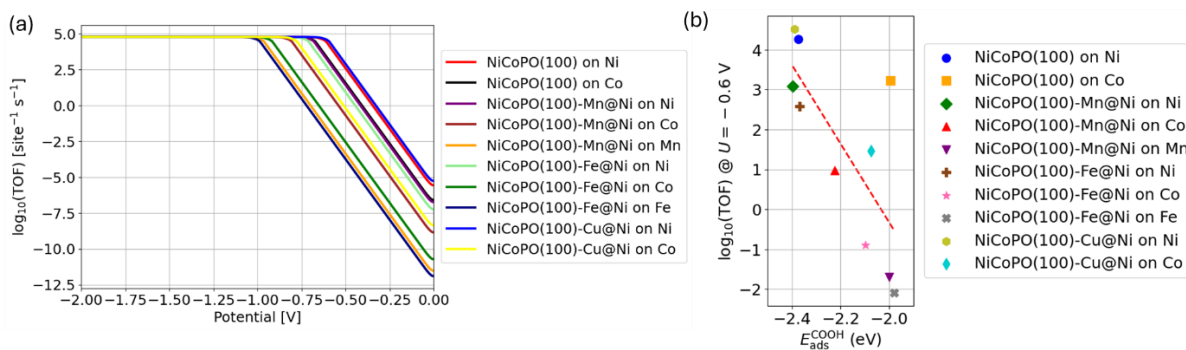

Figure 9 (a) TOF profiles for the CO_2RR to CO pathway and relationship between E_{ads}^{COOH} and log(TOF) (@U = -0.6 V).

CO₂RR to HCOOH

Similar to CO formation, the addition of transition metal doping alters the Gibbs free energy profile of the NiCoPO(100) surface during the reduction process for HCOOH formation. Notably, the CO_2RR process leading to HCOOH in the doped NiCoPO(100) system shows significant differences. In general, doping significantly reduces the U_L for HCOOH formation. Furthermore, unlike CO formation, the sites with the lowest U_L for HCOOH formation are the Co site and the transition metal M doping sites. The most substantial reduction in U_L is observed with Mn and Fe doping, indicating that CO_2RR activity toward HCOOH formation is greatly enhanced compared to the pure NiCoPO(100) surface.

Comparing the data in Tables 3 and 4, it is evident that the U_L for the CO_2RR process to HCOOH on the pure NiCoPO(100) surface is much higher than that for CO formation, indicating that the NiCoPO(100) catalyst generally favors CO production over HCOOH. This trend is also observed in most of the NiCoPO(100)-M systems. However, an interesting exception is found with NiCoPO(100)-Mn. On this surface, the CO_2RR process to HCOOH exhibits a U_L of -0.43 V, which

is significantly lower than the U_L for CO formation on the pure NiCoPO(100) surface (-0.61 V). This finding indicates that Mn doping not only significantly enhances the activity for HCOOH formation but also shifts the CO$_2$RR selectivity from CO production to HCOOH formation.

Interestingly, as in the case of CO formation, the thermodynamic determining step (TDS) for the CO$_2$RR to HCOOH is derived from a single reaction step, the reduction of CO$_2$ to HCOO (reaction 6), which has an endothermic profile, as shown in Figure 10. This indicates that the U_L for this process can be explained using the adsorption energy of the HCOO intermediate. Figures 11(a) and 11(b) present a comparison between E_{ads}^{HCOO}, U_L, and TOF for HCOOH formation. Similar to the case of CO production, the overall trend shows that stronger HCOO adsorption energies correspond to lower U_L values for HCOOH production. This observation is consistent with the Gibbs free energy profile of the CO$_2$RR process, where the reaction pathway is primarily governed by the free energy of HCOO intermediate formation. The plot clearly demonstrates that the Co site of NiCoPO(100)-Mn has the lowest U_L, as it maximizes the adsorption energy of the HCOO intermediate compared to the other active sites.

Table 4 Thermodynamics determining steps (TDS) and limiting potential U_L for CO$_2$RR to HCOOH.

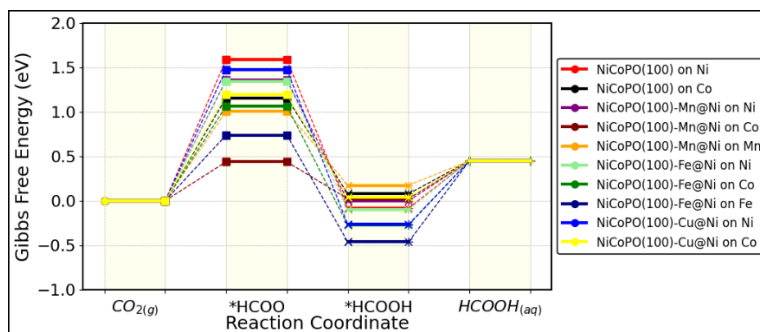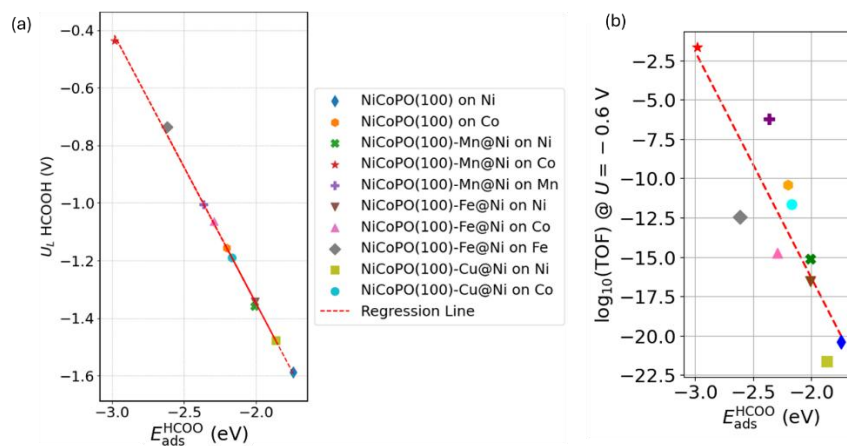| System	Site	TDS	U_L (V)
Ni$_3$Co$_3$(PO$_4$)$_4$	Ni	(6)	-1.58
	Co	(6)	-1.15
Ni$_3$Co$_3$(PO$_4$)$_4$-Mn@Ni	Ni	(6)	-1.35
	Co	(6)	-0.43
	Mn	(6)	-1.00
Ni$_3$Co$_3$(PO$_4$)$_4$-Fe@Ni	Ni	(6)	-1.34
	Co	(6)	-1.06
	Fe	(6)	-0.73
Ni$_3$Co$_3$(PO$_4$)$_4$-Cu@Ni	Ni	(6)	-1.47
	Co	(6)	-1.19

Figure 10 Free energy profiles for CO$_2$RR to HCOOH

Figure 11 Relation between E_{ads}^{HCOO} vs (a) U_L for CO$_2$RR to produce HCOOH and (b) log(TOF) (@U = -0.6 V).

The above discussion clearly indicates that incorporating transition metal dopants can substantially influence the limiting potential for HCOOH formation by enhancing HCOO adsorption. This behavior contrasts with that observed for CO formation, where doping does not improve the reaction. To rationalize this trend, we revisit the electronic structures of the isolated HCOO intermediate (Figure 7b) and the corresponding surfaces (Figure 8). Particular attention is given to the frontier molecular orbitals with p-orbital character on the oxygen atom, since HCOO adsorption involves the bonding of one oxygen atom from the intermediate with a transition metal atom on the surface (see Figures S1–S4 in the Supporting Information).

All molecular orbitals located near the Fermi level satisfy this condition. These orbitals appear at higher energies than those governing COOH adsorption, placing them closer to the d-orbitals of Ni, Co, and the transition metal dopants. This energy proximity facilitates stronger orbital hybridization with surface metal atoms compared to the COOH case. Consequently, transition metal dopants can more effectively tune the strength of HCOO adsorption, thereby promoting the reaction pathway for HCOOH formation.

Discussions

HER vs CO₂RR

In earlier studies, we discovered that the transition metal site is not necessarily the most stable for hydrogen atom adsorption (Blaylock et al., 2009; Nuruddin et al., 2023). As a result, determining the most stable adsorption site for H is critical before estimating the HER limiting potential on the NiCoPO(100) systems. The parameters for the most stable H adsorption on NiCoPO(100) and NiCoPO(100)-M surfaces are shown in Table 4 and Figure 12. According to the computed results, the O top site has the strongest H adsorption energy for all the surfaces, implying that the HER process will take place primarily at these O sites. In general, it can be observed that the U_L values for the HER process on NiCoPO(100) and NiCoPO(100)-M surfaces are very low. This indicates that the HER process is prone to occur on those surfaces.
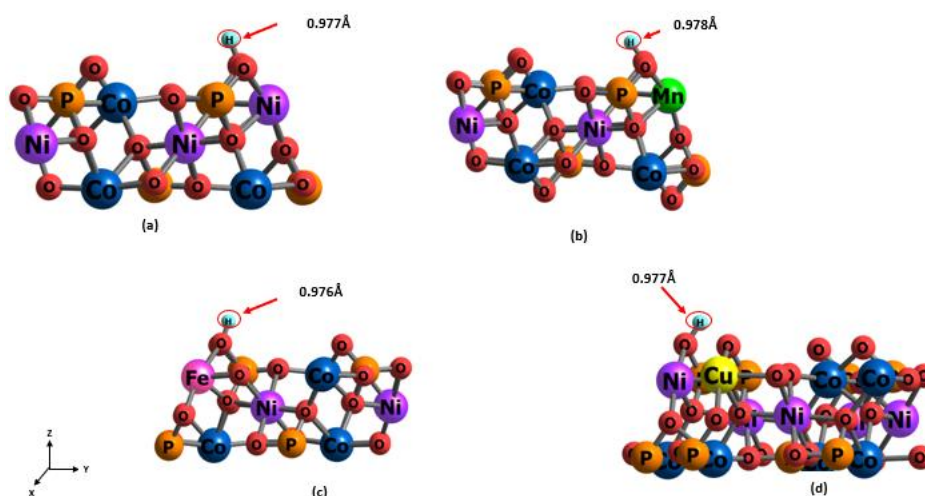

Figure 12   Geometries of the most stable H adsorption on the O site of (a) NiCoPO(100), (b) NiCoPO(100)-Mn@Ni, (c) NiCoPO(100)-Fe@Ni, and (d) NiCoPO(100)-Cu@Ni surfaces.

Table 5   H adsorption sites, adsorption energy, and HER limiting potential U_L^{HER} on NiCoPO(100) and NiCoPO(100)-M surfaces.

System	Site	E_{ads}^H(eV)	U_L^{HER} (V)
NiCoPO(100)	O@Ni	-0.26	-0.02
NiCoPO(100)-Mn@Ni	O@Ni	-0.11	-0.18
NiCoPO(100)-Fe@Ni	O@Fe	-0.07	-0.22
NiCoPO(100)-Cu@Ni	O@Ni	-0.46	-0.17

To investigate the effect of doping on the selectivity between HER and CO₂RR, it is essential to examine the difference in U_L values for these processes at the active surface sites under study. Figure 13a illustrates the difference in U_L for HER and CO₂RR to CO ($\Delta U_L^{[CO-HER]}$). Although it was previously noted that doping barely reduces the U_L value for CO formation (Table 3), the addition of dopants can slightly shift the selectivity between CO and HER for the NiCoPO(100)

surface. It is generally observed that the $\Delta U_{L}^{[CO-HER]}$ value at the Ni site decreases with the introduction of transition metal doping, particularly with Cu. This suggests that doping can slightly enhance the selectivity toward CO formation, even though it does not significantly reduce the U_L for CO formation.
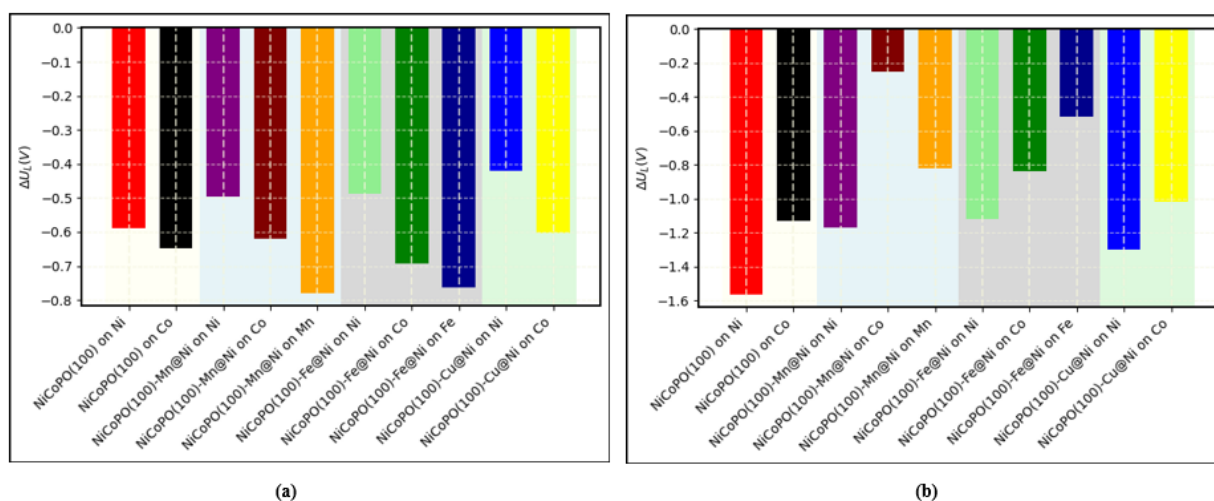

Figure 13   Graph of (a) ΔU_L (CO-HER) and (b) ΔU_L (HCOOH-HER)

Figure 13b presents the difference in U_L for HER and CO₂RR to HCOOH ($\Delta U_{L}^{[HCOOH-HER]}$). In this case, a more pronounced effect is observed compared to the CO formation scenario. Transition metal doping significantly shifts the $\Delta U_{L}^{[HCOOH-HER]}$ of the NiCoPO(100) surface, indicating that, in addition to enhancing CO₂RR activity for HCOOH by reducing the U_L, doping also shifts the selectivity of the system toward HCOOH formation. An interesting feature is observed at the Co site of NiCoPO(100)-Mn@Ni, where $\Delta U_{L}^{[HCOOH-HER]}$ reaches approximately -0.25 V. Although this still does not completely suppress the HER process, the inclusion of Mn doping significantly shifts the preference from HER toward CO₂RR for HCOOH formation on the NiCoPO(100) surface. Furthermore, as previously mentioned, the U_L for HCOOH formation in the Mn-doped case is much lower than the U_L for CO formation on the pure NiCoPO(100) surface, indicating a shift in selectivity from CO to HCOOH formation. Therefore, Mn doping is expected to enhance both the activity and selectivity of NiCoPO(100) for HCOOH production.

Conclusion

We have investigated the activity and selectivity of CO₂RR to CO and HCOOH on pure and transition metal-doped NiCoPO(100) surfaces using DFT-based calculations. Our findings indicate that doping with transition metals through substitutional defects can influence the trend of limiting potentials for the CO₂RR process. In general, transition metal doping (Mn, Fe, and Cu) does not significantly alter the CO formation activity compared to the pure NiCoPO(100) surface. However, these dopants substantially enhance the CO₂RR activity toward HCOOH production.

Interestingly, although the limiting potential for HCOOH formation is generally higher than for CO, suggesting that most NiCoPO(100) catalysts favor CO production, an exception is observed in the case of Mn doping. Here, the CO₂RR process energetically favors HCOOH formation over CO. Furthermore, while the majority of pure and transition metal-doped NiCoPO(100) surfaces struggle to suppress the parasitic HER process, Mn doping significantly shifts the energetic preference closer to HCOOH formation, reducing HER interference. These findings show that Mn-doped NiCoPO(100) catalysts provide an alternative pathway within Ni-based catalyst, where HCOOH emerges as the main product rather than CO.

Acknowledgement

Compliance with ethics guidelines

The authors declare they have no conflict of interest or financial conflicts to disclose.

This article contains no studies with human or animal subjects performed by the authors.

References

Alli, Y. A., Bamisaye, A., Bamidele, M. O., Etafo, N. O., Chkirida, S., Lawal, A., Hammed, V. O., Akinfenwa, A. S., Hanson, E., Nwakile, C., Kazeem, K. O., Ayanwunmi, R. J., Ige, A. S., Parga Torres, J. R., & Al Nageim, H. (2024). Transforming waste to wealth: Harnessing carbon dioxide for sustainable solutions. *Results in Surfaces and Interfaces*, 17, 100321. https://doi.org/10.1016/j.rsurfi.2024.100321

Alli, Y. A., Oladoye, P. O., Ejeromedoghene, O., Bankole, O. M., Alimi, O. A., Omotola, E. O., Olanrewaju, C. A., Philippot, K., Adeleye, A. S., & Ogunlaja, A. S. (2023). Nanomaterials as catalysts for CO2 transformation into value-added products: A review. *Science of The Total Environment*, *868*, 161547. https://doi.org/10.1016/j.scitotenv.2023.161547

Bi, W., Li, X., You, R., Chen, M., Yuan, R., Huang, W., Wu, X., Chu, W. S., Wu, C., & Xie, Y. (2018). Surface Immobilization of Transition Metal Ions on Nitrogen-Doped Graphene Realizing High-Efficient and Selective CO 2 Reduction. *Advanced Materials*, *30*, 1706617. https://doi.org/10.1002/adma.201706617

Blaylock, D. W., Ogura, T., Green, W. H., & Beran, G. J. O. (2009). Computational Investigation of Thermochemistry and Kinetics of Steam Methane Reforming on Ni(111) under Realistic Conditions. *The Journal of Physical Chemistry C, 113*(12), 4898–4908. https://doi.org/10.1021/jp806527q

Bolan, S., Padhye, L. P., Jasemizad, T., Govarthanan, M., Karmegam, N., Wijesekara, H., Amarasiri, D., Hou, D., Zhou, P., Biswal, B. K., Balasubramanian, R., Wang, H., Siddique, K. H. M., Rinklebe, J., Kirkham, M. B., & Bolan, N. (2024). Impacts of climate change on the fate of contaminants through extreme weather events. *Science of The Total Environment*, *909*, 168388. https://doi.org/10.1016/j.scitotenv.2023.168388

Calle-Vallejo, F., Martínez, J. I., & Rossmeisl, J. (2011). Density functional studies of functionalized graphitic materials with late transition metals for oxygen reduction reactions. *Phys. Chem. Chem. Phys.*, *13*(34), 15639–15643. https://doi.org/10.1039/C1CP21228A

Chen, Y., Zhang, J., Tian, J., Guo, Y., Xu, F., Zhang, Y., Wang, X., Yang, L., Wu, Q., & Hu, Z. (2023). Hierarchical Ni/N/C Single-Site Catalyst Achieving Industrial-Level Current Density and Ultra-Wide Potential Plateau of High CO Faradic Efficiency for CO2 Electroreduction. *Advanced Functional Materials*, *33*(20), 2214658. https://doi.org/10.1002/adfm.202214658

Darminto, R. P., Nuruzzahran, M. A., Syaifullah, D. A., Ilhami, H., Mobarak, N. N., AlMohamadi, H., Fathurrahman, F., Septiani, N. L. W., & Saputro, A. G. (2025). Influence of Transition Metal Doping on the Oxygen Evolution Reaction Activity of Nickel Phosphate Surface. *Langmuir*, *41*(16), 10205–10215. https://doi.org/10.1021/acs.langmuir.4c05130

El-Gohary, A. R. M., Galal, A., & Atta, N. F. (2023). CNTs/Graphene Oxide-Nickel Phosphate Nanocomposite-Based Electrochemical Sensor for Detecting H2O2 in Human Serum. *ChemistrySelect*, *8*(31), e202301922. https://doi.org/10.1002/slct.202301922

Ferriday, T. B., Middleton, P. H., & Kolhe, M. L. (2021). Review of the Hydrogen Evolution Reaction—A Basic Approach. *Energies*, *14*(24). https://doi.org/10.3390/en14248535

Giannozzi, P., Baroni, S., Bonini, N., Calandra, M., Car, R., Cavazzoni, C., Ceresoli, D., Chiarotti, G. L., Cococcioni, M., Dabo, I., Corso, A. D., de Gironcoli, S., Fabris, S., Fratesi, G., Gebauer, R., Gerstmann, U., Gougoussis, C., Kokalj, A., Lazzeri, M., … Wentzcovitch, R. M. (2009). QUANTUM ESPRESSO: a modular and open-source software project for quantum simulations of materials. *Journal of Physics: Condensed Matter*, *21*(39), 395502. https://doi.org/10.1088/0953-8984/21/39/395502

Grimme, S. (2006). Semiempirical GGA-type density functional constructed with a long-range dispersion correction. *Journal of Computational Chemistry*, *27*(15), 1787–1799. https://doi.org/10.1002/jcc.20495

Han, M. H., Kim, D., Kim, S., Yu, S.-H., Won, D. H., Min, B. K., Chae, K. H., Lee, W. H., & Oh, H.-S. (2022). Real-Time Mimicking the Electronic Structure of N-Coordinated Ni Single Atoms: NiS-Enabled Electrochemical Reduction of CO2 to CO. *Advanced Energy Materials*, *12*(35), 2201843. https://doi.org/10.1002/aenm.202201843

He, Q., Zhang, Y., Li, H., Yang, Y., Chen, S., Yan, W., Dong, J., Zhang, X.-M., & Fan, X. (2022). Engineering Steam Induced Surface Oxygen Vacancy onto Ni–Fe Bimetallic Nanocomposite for CO2 Electroreduction. *Small*, *18*(15), 2108034. https://doi.org/10.1002/smll.202108034

Hou, P., Wang, X., Wang, Z., & Kang, P. (2018). Gas Phase Electrolysis of Carbon Dioxide to Carbon Monoxide Using Nickel Nitride as the Carbon Enrichment Catalyst. *ACS Applied Materials & Interfaces*, *10*(44), 38024–38031. https://doi.org/10.1021/acsami.8b11942

Hua, W., Sun, H., Lin, L., Mu, Q., Yang, B., Su, Y., Wu, H., Lyu, F., Zhong, J., Deng, Z., & Peng, Y. (2022). A hierarchical Single-Atom Ni-N3-C catalyst for electrochemical CO2 reduction to CO with Near-Unity faradaic efficiency in a broad potential range. *Chemical Engineering Journal*, *446*, 137296. https://doi.org/10.1016/j.cej.2022.137296

Huang, J., Mensi, M., Oveisi, E., Mantella, V., & Buonsanti, R. (2019). Structural Sensitivities in Bimetallic Catalysts for Electrochemical CO2 Reduction Revealed by Ag–Cu Nanodimers. *Journal of the American Chemical Society*, *141*(6), 2490–2499. https://doi.org/10.1021/jacs.8b12381

Ikhwan, H., Syaifullah, D. A., Nuruzzahran, M. A., Mobarak, N. N., Wella, S. A., Fathurrahman, F., Septiani, N. L. W., & Saputro, A. G. (2025). Density functional study on the oxygen evolution reaction mechanism of transition metal doped bimetallic NiCu phosphate surface. *Computational and Theoretical Chemistry*, *1250*, 115304. https://doi.org/10.1016/j.comptc.2025.115304

Jeong, H.-Y., Balamurugan, M., Choutipalli, V. S. K., Jeong, E., Subramanian, V., Sim, U., & Nam, K. T. (2019). Achieving highly efficient CO2 to CO electroreduction exceeding 300 mA cm−2 with single-atom nickel electrocatalysts. *J. Mater. Chem. A*, *7*(17), 10651–10661. https://doi.org/10.1039/C9TA02405K

Kim, D., Xie, C., Becknell, N., Yu, Y., Karamad, M., Chan, K., Crumlin, E. J., Nørskov, J. K., & Yang, P. (2017). Electrochemical Activation of CO2 through Atomic Ordering Transformations of AuCu Nanoparticles. *Journal of the American Chemical Society*, *139*(24), 8329–8336. https://doi.org/10.1021/jacs.7b03516

Kumar, T., & Eswari J, S. (2023). Review and Perspectives of Emerging Green Technology for the Sequestration of Carbon Dioxide into Value-Added Products: An Intensifying Development. *Energy \& Fuels*, *37*(5), 3570–3589. https://doi.org/10.1021/acs.energyfuels.2c04122

Li, B., Meng, T. H., Meng, X. R., & Pang, H. (2021). Nickel/Cobalt phosphate ultrathin nanosheets grown on the surface of Fe(PO3)3 nanosheets for high performance supercapacitors. *Journal of Energy Storage*, *42*, 103082. https://doi.org/10.1016/j.est.2021.103082

Li, J., Chen, W., Lin, R., Huang, M., Wang, M., Chai, M., & Zhu, H. (2021). Thermally Evaporated Ag–Au Bimetallic Catalysts for Efficient Electrochemical CO2 Reduction. *Particle \& Particle Systems Characterization*, *38*(11), 2100148. https://doi.org/10.1002/ppsc.202100148

Li, M., Yang, K., Sun, Y., Gao, T., Nie, Z., Chen, S., Li, Q., & Duan, J. (2024). Local Steric Hindrance for CO2 Electroreduction at a Thermodynamic Potential and Wide Working Window. *Advanced Energy Materials*, *14*(10), 2303073. https://doi.org/10.1002/aenm.202303073

Li, X., Bi, W., Chen, M., Sun, Y., Ju, H., Yan, W., Zhu, J., Wu, X., Chu, W., Wu, C., & Xie, Y. (2017). Exclusive Ni–N4 Sites Realize Near-Unity CO Selectivity for Electrochemical CO2 Reduction. *Journal of the American Chemical Society*, *139*(42), 14889–14892. https://doi.org/10.1021/jacs.7b09074

Liu, X.-H., Jia, X.-L., Zhao, Y.-L., Zheng, R.-X., Meng, Q.-L., Liu, C.-P., Xing, W., & Xiao, M.-L. (2023). Recent advances in nickel-based catalysts for electrochemical reduction of carbon dioxide. *Advanced Sensor and Energy Materials*, *2*(3), 100073. https://doi.org/10.1016/j.asems.2023.100073

Ma, X., Sun, F., Qin, L., Liu, Y., Kang, X., Wang, L., Jiang, D., Tang, Q., & Tang, Z. (2022). Electrochemical CO2 reduction catalyzed by atomically precise alkynyl-protected Au7Ag8{,} Ag9Cu6{,} and Au2Ag8Cu5 nanoclusters: probing the effect of multi-metal core on selectivity. *Chem. Sci.*, *13*(34), 10149–10158. https://doi.org/10.1039/D2SC02886G

Ma, Z., Wan, T., Zhang, D., Yuwono, J. A., Tsounis, C., Jiang, J., Chou, Y.-H., Lu, X., Kumar, P. V, Ng, Y. H., Chu, D., Toe, C. Y., Han, Z., & Amal, R. (2023). Atomically Dispersed Cu Catalysts on Sulfide-Derived Defective Ag Nanowires for Electrochemical CO2 Reduction. *ACS Nano*, *17*(3), 2387–2398. https://doi.org/10.1021/acsnano.2c09473

Maulana, A. L., Putra, R. I. D., Saputro, A. G., Agusta, M. K., Nugraha, N., & Dipojono, H. K. (2019). DFT and Microkinetic Investigation of Methanol Synthesis via CO 2 Hydrogenation on Ni(111)-based Surfaces. *Physical Chemistry Chemical Physics*, *21*(111), 20276–20286. https://doi.org/10.1039/C9CP02970B

Maulana, A. L., Saputro, A. G., Prasetyo, Y., Mahyuddin, M. H., Iqbal, M., Yudistira, H. T., Wenten, I. G., & Dipojono, H. K. (2021). Two-Electron Electrochemical Reduction of CO2 on B-Doped Ni–N–C Catalysts: A First-Principles Study. *The Journal of Physical Chemistry C*, *125*(2), acs.jpcc.1c04986. https://doi.org/10.1021/acs.jpcc.1c04986

Moore, T. R., Damon Matthews, H., & Chavaillaz, Y. (2024). Linking Historical and Projected Trends in Extreme Precipitation with Cumulative Carbon Dioxide Emissions. *Atmosphere-Ocean*, *62*(2), 165–182. https://doi.org/10.1080/07055900.2023.2259328

Niu, Y., Zhang, C., Wang, Y., Fang, D., Zhang, L., & Wang, C. (2021). Confining Chainmail-Bearing Ni Nanoparticles in N-doped Carbon Nanotubes for Robust and Efficient Electroreduction of CO2. *ChemSusChem*, *14*(4), 1140–1154. https://doi.org/10.1002/cssc.202002596

Norskov, J., Rossmeisl, J., Logadottir, A., Lindqvist, L., Kitchin, J. R., Bligaard, T., & Jonsson, H. (2004). Origin of the overpotential for oxygen reduction at a fuel-cell cathode. *The Journal of Physical Chemistry B*, *108*(46), 17886–17892. https://doi.org/10.1021/jp047349j

Nuruddin, A., Saputro, A. G., Maulana, A. L., Fajrial, A. K., Shukri, G., Mahyuddin, M. H., Aprilyanti, F. D., Harimawan, A., & Dipojono, H. K. (2023). Enhancing oxygen reduction reaction activity of pyrolyzed Fe–N–C catalyst by the inclusion of BN dopant at the graphitic edges. *Applied Surface Science*, *608*, 155203. https://doi.org/10.1016/j.apsusc.2022.155203

Nuruddin, A., Saputro, A. G., Maulana, A. L., Rusydi, F., Akbar, F. T., Yudistira, H. T., & Dipojono, H. K. (2024). Selectivity of CO2 reduction reaction to CO on the graphitic edge active sites of Fe-single-atom and dual-atom catalysts: A combined DFT and microkinetic modeling. *Carbon Resources Conversion*, *7*(1), 100185. https://doi.org/10.1016/j.crcon.2023.05.004

Nuruzzahran, M. A., Syaifullah, D. A., Mariani, C. C., Fathurrahman, F., Yuliarto, B., Dipojono, H. K., AlMohamadi, H., Wella, S. A., Wulan Septiani, N. L., & Saputro, A. G. (2025). Oxygen evolution reaction activity of Ni3(PO4)2 and bimetallic Ni3M3(PO4)4 (M = Mn, Fe, Co): Insights from DFT and experimental validation. *Fuel*, *385*, 134183. https://doi.org/10.1016/j.fuel.2024.134183

Perdew, J. P., Burke, K., & Ernzerhof, M. (1996). Generalized Gradient Approximation Made Simple. *Phys. Rev. Lett.*, *77*(18), 3865–3868. https://doi.org/10.1103/PhysRevLett.77.3865

Peterson, A. A., Abild-Pedersen, F., Studt, F., Rossmeisl, J., & Nørskov, J. K. (2010). How copper catalyzes the electroreduction of carbon dioxide into hydrocarbon fuels. *Energy Environ. Sci.*, *3*(9), 1311–1315. https://doi.org/10.1039/C0EE00071J

Qian, L., & Miao, Y. (2019). Nanosheet organized flower-like Co/Zn phosphate on nickel foam for efficient water splitting in both acid and basic solutions. *Polyhedron*, *160*, 213–218. https://doi.org/10.1016/j.poly.2018.12.050

Saputro, A. G., Maulana, A. L., Aprilyanti, F. D., & Dipojono, H. K. (2021a). Theoretical Study of Direct Carbon Dioxide Conversion to Formic Acid on Transition Metal-doped Subnanometer Palladium Clusters. *Journal of Engineering and Technological Sciences*, *53*(4), 210402. https://doi.org/10.5614/j.eng.technol.sci.2021.53.4.2

Saputro, A. G., Maulana, A. L., Fathurrahman, F., Shukri, G., Mahyuddin, M. H., Agusta, M. K., Wungu, T. D. K., & Dipojono, H. K. (2021b). Density functional and microkinetic study of CO2 hydrogenation to methanol on subnanometer Pd cluster doped by transition metal (M= Cu, Ni, Pt, Rh). *International Journal of Hydrogen Energy*, *46*(27), 14418–14428. https://doi.org/10.1016/j.ijhydene.2021.02.009

Saxena, A., Liyanage, W. P. R., Kapila, S., & Nath, M. (2022). Nickel selenide as an efficient electrocatalyst for selective reduction of carbon dioxide to carbon-rich products††Electronic supplementary information (ESI) available: GC-TCD spectra, product quantification details from NMR spectra, calculation of farada. *Catalysis Science & Technology*, *12*(15), 4727–4739. https://doi.org/10.1039/d2cy00583b

Septiani, N. L. W., Kaneti, Y. V., Fathoni, K. B., Guo, Y., Ide, Y., Yuliarto, B., Jiang, X., Nugraha, Dipojono, H. K., Golberg, D., & Yamauchi, Y. (2020a). Tailorable nanoarchitecturing of bimetallic nickel–cobalt hydrogen phosphate via the self-weaving of nanotubes for efficient oxygen evolution. *J. Mater. Chem. A*, *8*(6), 3035–3047. https://doi.org/10.1039/C9TA13442E

Septiani, N. L. W., Kaneti, Y. V., Fathoni, K. B., Kani, K., Allah, A. E., Yuliarto, B., Nugraha, Dipojono, H. K., Alothman, Z. A., Golberg, D., & Yamauchi, Y. (2020b). Self-Assembly of Two-Dimensional Bimetallic Nickel–Cobalt Phosphate Nanoplates into One-Dimensional Porous Chainlike Architecture for Efficient Oxygen Evolution Reaction. *Chemistry of Materials*, *32*(16), 7005–7018. https://doi.org/10.1021/acs.chemmater.0c02385

Shaikh, A. R., Vidal-López, A., Brotons-Rufes, A., Pajski, J. J., Zafar, S., Mahmood, R. A., Khan, M. U., Poater, A., Chawla, M., & Cavallo, L. (2024). Amino acid ionic liquids as efficient catalysts for CO2 capture: A combined static and dynamic approach. *Results in Surfaces and Interfaces*, *14*, 100175. https://doi.org/10.1016/j.rsurfi.2023.100175

Syaifullah, D. A., Nuruzzahran, M. A., Idhola, R. D., Mobarak, N. N., AlMohamadi, H., Patole, S., Wella, S. A., Akbar, F. T., Rizkiana, J., Wulan Septiani, N. L., & Saputro, A. G. (2026). Tuning oxygen evolution activity via transition metal doping in bimetallic nickel phosphates. *Applied Surface Science*, *717*, 164846. https://doi.org/10.1016/j.apsusc.2025.164846

Tan, D., Cui, C., Shi, J., Luo, Z., Zhang, B., Tan, X., Han, B., Zheng, L., Zhang, J., & Zhang, J. (2019). Nitrogen-carbon layer coated nickel nanoparticles for efficient electrocatalytic reduction of carbon dioxide. *Nano Research*, *12*(5), 1167–1172. https://doi.org/10.1007/s12274-019-2372-1

Tripkovic, V., Vanin, M., Karamad, M., Björketun, M. E., Jacobsen, K. W., Thygesen, K. S., & Rossmeisl, J. (2013). Electrochemical CO2 and CO Reduction on Metal-Functionalized Porphyrin-like Graphene. *The Journal of Physical Chemistry C*, *117*(18), 9187–9195. https://doi.org/10.1021/jp306172k

Wang, D., Wang, Y., Fu, Z., Xu, Y., Yang, L.-X., Wang, F., Guo, X., Sun, W., & Yang, Z.-L. (2021). Cobalt–Nickel Phosphate Composites for the All-Phosphate Asymmetric Supercapacitor and Oxygen Evolution Reaction. *ACS Applied Materials \& Interfaces*, *13*(29), 34507–34517. https://doi.org/10.1021/acsami.1c04614

Wijayanti, D. P., Nuruzzahran, M. A., Syaifullah, D. A., Adhika, D. R., AlMohamadi, H., Mobarak, N. N., Septiani, N. L. W., & Saputro, A. G. (2025). Hydrogen evolution reaction mechanism on pristine and defective nickel phosphate surfaces. *Results in Surfaces and Interfaces*, *18*, 100431. https://doi.org/10.1016/j.rsurfi.2025.100431

Xu, C., Vasileff, A., Jin, B., Wang, D., Xu, H., Zheng, Y., & Qiao, S.-Z. (2020). Graphene-encapsulated nickel–copper bimetallic nanoparticle catalysts for electrochemical reduction of CO2 to CO. *Chem. Commun.*, *56*(76), 11275–11278. https://doi.org/10.1039/D0CC04779A

Yang, K., Li, M., Gao, T., Xu, G., Li, D., Zheng, Y., Li, Q., & Duan, J. (2024). An acid-tolerant metal-organic framework for industrial CO2 electrolysis using a proton exchange membrane. *Nature Communications*, *15*(1). https://doi.org/10.1038/s41467-024-51475-7

Yusuf, N., Almomani, F., & Qiblawey, H. (2023). Catalytic CO2 conversion to C1 value-added products: Review on latest catalytic and process developments. *Fuel*, *345*, 128178. https://doi.org/10.1016/j.fuel.2023.128178

Zhang, X., Shang, N., Gao, S., Wang, C., Gao, Y., & Wang, Z. (2019). Surfactant assisted self-assembly of NiCo phosphate with superior electrochemical performance for supercapacitor. *Applied Surface Science*, *483*, 529–535. https://doi.org/10.1016/j.apsusc.2019.03.339

Zhang, Y., He, Z., Dong, Q., Tang, X., Yang, L., Huang, K., Zou, Z., Jiang, X., & Xiong, X. (2022). 3D CoxP@NiCo-LDH heteronanosheet array: As a high sensitivity sensor for glucose. *Microchemical Journal*, *172*, 106923. https://doi.org/10.1016/j.microc.2021.106923

Zhao, H., & Yuan, Z.-Y. (2020). Insights into Transition Metal Phosphate Materials for Efficient Electrocatalysis. *ChemCatChem*, *12*(15), 3797–3810. https://doi.org/10.1002/cctc.202000360

Zhao, R., Wang, Y., Ji, G., Zhong, J., Zhang, F., Chen, M., Tong, S., Wang, P., Wu, Z., Han, B., & Liu, Z. (2023). Partially Nitrided Ni Nanoclusters Achieve Energy-Efficient Electrocatalytic CO2 Reduction to CO at Ultralow Overpotential. *Advanced Materials*, *35*(5), 2205262. https://doi.org/10.1002/adma.202205262

Zhao, S., Xiao, N., Li, H., Guo, Z., Bai, J., Xiao, J., Guo, H., Ma, X., & Qiu, J. (2021). A nickel-nitrogen-doped carbon foam as monolithic electrode for highly efficient CO2 electroreduction. *Journal of CO2 Utilization*, *49*, 101549. https://doi.org/10.1016/j.jcou.2021.101549

Zheng, T., Jiang, K., Ta, N., Hu, Y., Zeng, J., Liu, J., & Wang, H. (2019). Large-Scale and Highly Selective CO2 Electrocatalytic Reduction on Nickel Single-Atom Catalyst. *Joule*, *3*(1), 265–278. https://doi.org/10.1016/j.joule.2018.10.015

Zhou, C., Gao, T., Wang, Y., Liu, Q., & Xiao, D. (2019). Through a hydrothermal phosphatization method synthesized NiCo and Fe-based electrodes for high-performance battery-supercapacitor hybrid device. *Applied Surface Science*, *475*, 729–739. https://doi.org/10.1016/j.apsusc.2018.12.299